Mono-everything: Combined limits on dark matter production at colliders from multiple final states

Zhou, N.; Berge, D.; Whiteson, D.

DOI
10.1103/PhysRevD.87.095013

Publication date
2013

Document Version
Final published version

Published in
Physical Review D. Particles, Fields, Gravitation, and Cosmology

PHYSICAL REVIEW D **87,** 095013 (2013)

Mono-everything: Combined limits on dark matter production at colliders from multiple final states

Ning Zhou,[1] David Berge,[2] and Daniel Whiteson[1]

[1]*Department of Physics and Astronomy, University of California, Irvine, California 92697, USA*
[2]*Gravitation AstroParticle Physics Amsterdam, University of Amsterdam, Amsterdam 1098 XH, Netherlands*

(Received 14 February 2013; published 22 May 2013)

Searches for dark matter production at particle colliders are complementary to direct-detection and indirect-detection experiments and especially powerful for small masses, $m_\chi < 100$ GeV. An important collider dark matter signature is due to the production of a pair of these invisible particles with the initial-state radiation of a standard model particle. Currently, collider searches use individual and nearly orthogonal final states to search for initial-state jets, photons or massive gauge bosons. We combine these results across final states and across experiments to give the strongest current collider-based limits in the context of effective field theories and map these to limits on dark matter interactions with nuclei and to dark matter self-annhiliation.

DOI: 10.1103/PhysRevD.87.095013 PACS numbers: 12.60.−i, 95.30.Cq

Although the presence of dark matter in the Universe has been well-established, little is known of its particle nature or its nongravitational interactions. A vibrant experimental program is searching for a weakly interacting massive particle (WIMP), denoted as χ, and interactions with standard model particles via some as-yet-unknown mediator. If the mediator is too heavy to be resolved, the interaction can be modeled as an effective field theory with a four-point interaction.

One critical component of this program is the search for pair production of WIMPs at particle colliders, specifically $pp \to \chi\bar{\chi}$ at the LHC via some unknown intermediate state. As the final-state WIMPs are invisible to the detectors, the events can only be seen if there is associated initial-state radiation of a standard model particle [1–3], see Fig. 1, recoiling against the dark matter pair.

The LHC collaborations have reported limits on the cross section of $pp \to \chi\bar{\chi} + X$ where X is a gluon or quark [4,5], photon [6,7], and other searches have been repurposed to study the cases where X is a W [8] or Z boson [9,10]. In each case, limits are reported in terms of the mass scale $M_\star$ of the unknown interaction expressed in an effective field theory [1–3,11–19]. These various initial-state tags probe the same effective theory but are largely statistically independent due to their nearly orthogonal event selection requirements. As the relative rates of radiation of gluons (quarks), photons, W or Z bosons from the incoming quark (gluon) legs are determined by the standard model, the various probes may be combined to give the strongest limits without any loss of generality or additional theoretical assumptions.

Recently, an analysis of multijet final states was shown to add some sensitivity to the monojet analyses [20]; that sample is not statistically independent from the monojet results used here and is not included. An earlier global analysis of indirect and direct constraints with Tevatron data and monojet data from ATLAS provided an initial set of combined constraints [21] using the approximations of a χ^2 technique.

In this paper, we perform a full statistical combination of the limits from all available channels (monojet, monophoton and mono-Z[1] from both ATLAS and CMS at $\sqrt{s} = 7$ TeV, accounting for the dominant correlations and providing the most powerful current collider constraints. While the limits reported by the experimental collaborations are typically given for a few select effective operators, we calculate the efficiencies of their selections and reinterpret their searches for the complete set of operators relevant for Dirac fermion or complex scalar WIMPs.

I. MODELS

The effective theories of dark matter considered here consider the possibility that the final-state WIMPs are a Dirac fermion (operators D1-D14 in Ref. [14]) or a complex scalar (operators C1-C6 in Ref. [14]). These four-point effective operators assume that the unknown intermediate particles have a heavy mass scale; we use a suppression scale, $M_\star$. Cross sections at leading order for production in pp collisions at $\sqrt{s} = 7$ TeV are shown in Fig. 2 for select operators with $M_\star = 1$ TeV for illustration. Recently, next-to-leading-order calculations have been performed for monojet and monophoton processes [23] showing ratios of $\sigma_{\rm NLO}/\sigma_{\rm LO} \approx 1.2$–$1.5$; our monojet results partially include this effect by generating and matching multiple-parton emission.

For some operators, cross sections of dark matter production at the LHC can be transformed into cross sections for WIMP-nucleon interaction, $\sigma(\chi - n)$ [3], or WIMP

[1]Final states with a heavy boson have little power relative to the monophoton or monojet; we include mono-Z as a demonstration and do not include mono-W, although see Ref. [8]. For an alternative view of mono-Z, see Ref. [22].

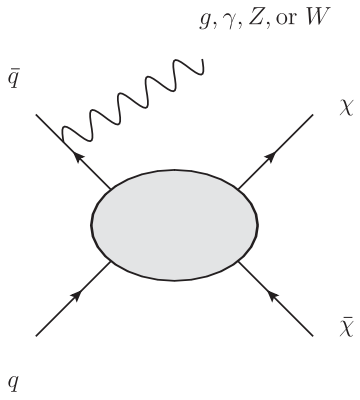

FIG. 1. Pair production of WIMPs ($\chi\bar{\chi}$) in proton-proton collisions at the LHC via an unknown intermediate state, with initial-state radiation of a standard model particle.

annihilations [2]. Therefore, the effective field theories allow us to map measurements performed at the LHC to the quantities relevant for direct-detection and indirect-detection dark matter search experiments.

The effective-field-theory approach is valid as long as the unknown new mediator particles that couple the dark-matter particles to standard model quarks or gluons are too heavy to be resolved: $q < M^*$, where q is the momentum transfer. The breakdown of the effective approach depends ultimately on the details of the new and unknown physics, specifically on the number of new mediator particles and the new couplings. Therefore, these theories cannot be treated generically and must be interpreted with some care. To guide the interpretation, we indicate the range of validity as lower bounds on the mass suppression scale $M_\star$ following Ref. [3]. We note that any range of validity of the effective field theory involves assumptions about the unknown physics; see Refs. [20,24] for additional unitarity arguments and more stringent validity ranges.

Assuming the simplest possible structure of new physics (mediation via exactly one new heavy mediator of mass M, $M_\star = M/\sqrt{g_1 g_2}$, g_1 and g_2 being coupling constants), bounds on the suppression scale can be placed by requiring $M > 2m_\chi$ and that the new physics be as strongly coupled as possible for it to be still perturbative ($\sqrt{g_1 g_2} < 4\pi$):

$$M_\star > \frac{m_\chi}{2\pi}\,(\text{D5 to D14 and C3 to C6}),$$

$$\sqrt{\frac{M_\star^3}{m_q}} > \frac{m_\chi}{2\pi}\,(\text{D1 to D4}), \qquad \frac{M_\star^2}{m_q} > \frac{m_\chi}{2\pi}\,(\text{C1 and C2}).$$

Note that we are accounting for additional factors of m_q in the definitions of operators D1 to D4 and C1, C2 of Ref. [3].

II. EXPERIMENTAL SEARCHES

The experimental searches typically require one or more high-p_T object and missing transverse momentum; see Table I for a summary and comparison of the monophoton and monojet selections.

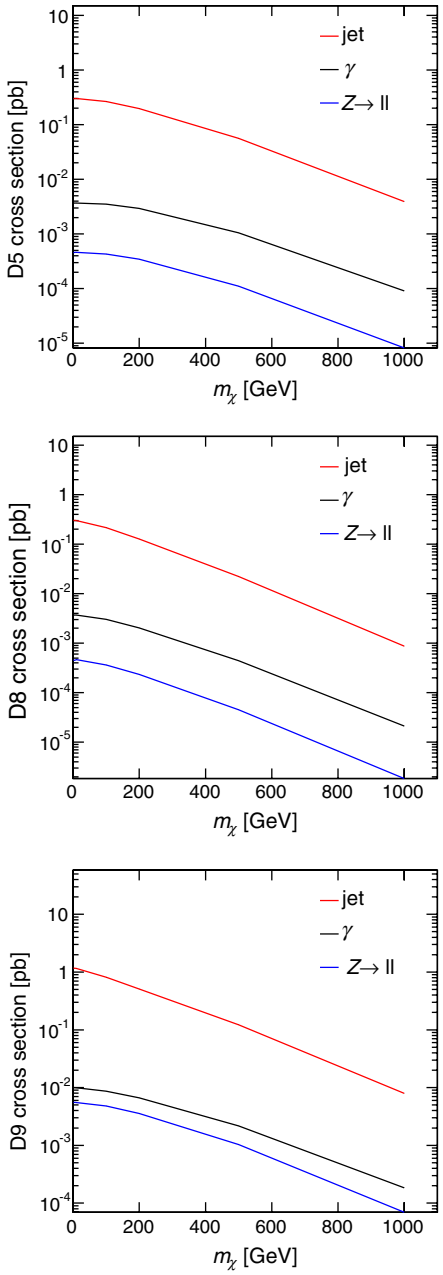

FIG. 2 (color online). Cross sections for $pp \to \chi\bar{\chi} + X$ production where X is the initial-state radiation of a jet, photon or Z boson. Jet and photon final states include a $p_T > 80$ GeV cut at the parton level. Each pane shows the cross section for a different effective operator: the top is D5, the center is D8, and the bottom is D9. See Ref. [3] for operator definitions.

The mono-Z analysis [10] uses the ATLAS $ZZ \to \ell\ell\nu\nu$ cross-section measurement [9], which requires:

(i) two same-flavor opposite-sign electrons or muons, each with $p_T^\ell > 20$ GeV, $|\eta^\ell| < 2.5$;

(ii) dilepton invariant mass close to the Z-boson mass: $m_{\ell\ell} \in [m_Z - 15, m_Z + 15]$ GeV;

TABLE I. Summary of event selection requirements in ATLAS and CMS monojet or monophoton analyses. Note that ATLAS uses two signal regions ($\not{E}_T > 350$ or 500 GeV) for the monojet analyses, depending on the operator.

	ATLAS	CMS
jet	1 or 2 jets	1 or 2 jets
	$p_{\mathrm{T}}^{j_1} > 350(500)$ GeV	$p_{\mathrm{T}}^{j_1} > 110$ GeV
	$p_{\mathrm{T}}^{j_2} > 30$ GeV	$p_{\mathrm{T}}^{j_2} > 30$ GeV
	$\not{E}_T > 350(500)$ GeV	$\not{E}_T > 350$ GeV
	veto leptons	veto leptons
	$\Delta\phi(j_2, \not{E}_T) > 0.5$	$\Delta\phi(j_1, j_2) < 2.5$
γ	1 photon, $p_{\mathrm{T}} > 150$ GeV	1 photon $p_{\mathrm{T}} > 145$ GeV
	$\not{E}_T > 150$ GeV	$\not{E}_T > 130$ GeV
	≤ 1 jet with $p_{\mathrm{T}} > 30$ GeV	0 track with $p_T > 20$ GeV
	isolation details	isolation details
	$\Delta\phi(\gamma, \not{E}_T) > 0.4$	
	$\Delta\phi(j_1, \not{E}_T) > 0.4$	
	veto leptons	

(iii) no particle-level jet with $p_{\mathrm{T}}^{j} > 25$ GeV and $|\eta^j| < 4.5$;
(iv) $(|p_{\mathrm{T}}^{\nu\bar{\nu}} - p_{\mathrm{T}}^{Z}|)/p_{\mathrm{T}}^{Z} < 0.6$;
(v) $-p_{\mathrm{T}}^{\nu\bar{\nu}} \times \cos(\Delta\phi(p_{\mathrm{T}}^{\nu\bar{\nu}}, p_{\mathrm{T}}^{Z})) > 80$ GeV.

The selection efficiency of each selection for each operator is given in Table II and was estimated in the following way. References [4–7] provide signal efficiency for several select operators; this efficiency is the product of geometric and kinematic acceptance of the selection criteria and object reconstruction efficiency. The object reconstruction efficiency depends on the details of the detector performance but is largely independent of the operator. The geometric and kinematic acceptances can be reliably estimated using parton-level simulated event samples [25]. We measure the geometric and kinematic efficiency for each operator and use the quoted total efficiencies to deduce the object reconstruction efficiencies. This allows us to estimate the total efficiency for each operator.

III. COMBINATION

The separate analyses, each of which are single-bin counting experiments, are combined into a multibin counting experiment. This allows for a coherent signal rate to be tested across channels but preserves their distinct signal-to-background ratios.

The background estimates are taken directly from the experimental publications, see a summary in Table III, and are assumed to be uncorrelated across channels, as they are typically dominated by channel-specific or detector-specific uncertainties. For example, in some cases, the background estimates are data-driven, and the dominant uncertainties are in the finite statistics of independent control samples. Inclusion of correlations up to 20% does not qualitatively impact the results of the combination.

TABLE II. Selection efficiency as percentages for each channel of the analyses used in the combination, for operators D1–14 and C1–C6 for low and high values of the WIMP mass m_χ. The ATLAS monojet analysis has two signal regions; we use $\not{E}_T >$ 500(350) GeV and the $p_{\mathrm{T}}^{j_1} > 500(350)$ GeV region for operators D9–D14 (D1–D8 and C1–C6). Operators D11–14, C5 and C6 only couple to gluon initial states and so have no efficiency for photon or Z-boson radiation. The Z efficiencies include the $Z \to \ell\ell$ branching fraction. Jet and photon samples include a $p_T > 80$ GeV cut at parton level.

		ATLAS			CMS	
Operator	m_χ	jet	γ	Z	jet	γ
D1	10	0.4%	11.2%	1.2%	0.7%	8.0%
	1000	2.6%	19.1%	1.2%	3.6%	11.3%
D2	10	0.4%	10.8%	1.2%	0.7%	8.0%
	1000	2.4%	18.6%	1.1%	3.7%	11.3%
D3	10	0.5%	11.1%	1.2%	0.7%	8.0%
	1000	2.6%	18.9%	1.2%	3.9%	11.3%
D4	10	0.5%	10.8%	1.2%	0.7%	7.6%
	1000	2.6%	18.6%	1.1%	3.7%	11.3%
D5	10	1.7%	18.2%	0.9%	2.2%	11.3%
	1000	3.3%	23.5%	1.1%	4.5%	14.7%
D6	10	1.7%	18.7%	0.9%	2.2%	12.0%
	1000	3.2%	23.6%	1.1%	4.4%	15.2%
D7	10	1.7%	18.1%	0.9%	2.4%	11.3%
	1000	3.3%	23.4%	1.1%	4.4%	14.5%
D8	10	1.7%	18.5%	0.9%	2.3%	11.8%
	1000	3.1%	23.6%	1.1%	4.3%	15.1%
D9	10	0.9%	23.5%	1.4%	4.1%	14.1%
	1000	1.2%	23.3%	1.4%	5.1%	14.8%
D10	10	1.1%	23.6%	1.4%	4.2%	14.4%
	1000	1.2%	23.4%	1.4%	5.2%	14.8%
D11	10	0.9%	...	...	4.1%	...
	1000	2.4%	...	...	7.5%	...
D12	10	1.0%	...	...	4.2%	...
	1000	2.4%	...	...	7.4%	...
D13	10	0.9%	...	...	4.1%	...
	1000	2.4%	...	...	7.5%	...
D14	10	1.1%	...	...	4.0%	...
	1000	2.4%	...	...	7.4%	...
C1	10	0.1%	7.0%	1.0%	0.2%	5.3%
	1000	2.3%	18.2%	1.1%	3.3%	11.0%
C2	10	0.1%	7.0%	1.0%	0.1%	5.6%
	1000	2.5%	18.4%	1.1%	3.8%	11.2%
C3	10	1.7%	18.4%	0.9%	2.3%	11.6%
	1000	2.9%	23.6%	1.1%	4.1%	14.9%
C4	10	1.4%	18.4%	0.9%	2.2%	11.8%
	1000	3.0%	23.8%	1.1%	4.1%	15.3%
C5	10	1.4%	...	...	1.7%	...
	1000	5.9%	...	...	7.6%	
C6	10	1.2%	...	...	1.7%	...
	1000	5.9%	...	...	7.6%	...

TABLE III. 90% C.L. limits on N_{events}, efficiencies for $m_\chi = 10$ GeV and limits on $\sigma(pp \to \chi\bar{\chi} + X)$ using the D5 operator. In the case of the $Z + \not{E}_T$ final state, the efficiency is relative to $Z \to \ell\ell$ decays only.

Channel	Background	Observed	Limit N	Efficiency	Luminosity (fb^{-1})	Limit σ (fb)
ATLAS jet + $\not{E}_T$	750 ± 60	785	139.3	1.7%	4.8	1,700
CMS jet + $\not{E}_T$	1225 ± 101	1142	125.2	2.2%	5.0	1,140
ATLAS γ + $\not{E}_T$	137 ± 20	116	27.4	18%	4.6	33
CMS γ + $\not{E}_T$	75.1 ± 9.4	73	19.3	11%	5.0	35
ATLAS Z + $\not{E}_T$	86.2 ± 7.2	87	21.7	13%	4.6	36

TABLE IV. 90% C.L. limits on N_{events}, efficiencies for $m_\chi = 10$ GeV and limits on $\sigma(pp \to \chi\bar{\chi} + X)$ using the D9 operator.

Channel	Background	Observed	Limit N	Efficiency	Luminosity (fb^{-1})	Limit σ (fb)
ATLAS jet + $\not{E}_T$	83 ± 14	77	25.5	0.9%	4.8	590
CMS jet + $\not{E}_T$	1225 ± 101	1142	125.2	4.1%	5.0	610

The backgrounds, their uncertainties and the observed yield can be used to calculate a 90% C.L. upper limit on the number of signal events N in the sample, see Tables III and IV, using the C.L.s method [26,27]. This value is almost completely model-independent. Translating it into a limit on the cross section for the $pp \to \chi\bar{\chi} + X$ signal requires the efficiency of the signal in each selection; see Table III. These individual limits reproduce well the results reported by the experiments.

The signal regions are nearly orthogonal but not exactly. For example, the monojet analyses do not veto events with a photon, and the monophoton analyses allow the presence of one jet. From our parton-level simulated event samples, we estimated the overlaps among different channels and found that the overlap fraction is less than 1%.

The individual analyses include signal uncertainties of up to 20% on the cross section, mostly due to uncertainties in jet energy calibration and levels of initial-state radiation. These uncertainties do not affect the cross-section limits but can be simply applied to limits on $M_\star$. In each case, we quote the limit using the central value.

To summarize, the assumptions made in this combination are

TABLE V. 90% C.L. limits on $\sigma(pp \to \chi\bar{\chi} + X)$ for $m_\chi = 10$ GeV, theory prediction for $M_\star = 1$ TeV, and limits on $M_\star$ using the D5 operator. In the case of the $Z + \not{E}_T$ final state, the predictions include the $Z \to \ell\ell$ branching fraction.

Channel	Limit σ (fb)	Predicted (fb)	Limit $M_\star$ (GeV)		
ATLAS jet + $\not{E}_T$	1,700	370	685	785	795
CMS jet + $\not{E}_T$	1,140	370	750		
ATLAS γ + $\not{E}_T$	33	3.7	580	645	
CMS γ + $\not{E}_T$	35	3.7	570		
ATLAS Z + $\not{E}_T$	36	0.5	340		

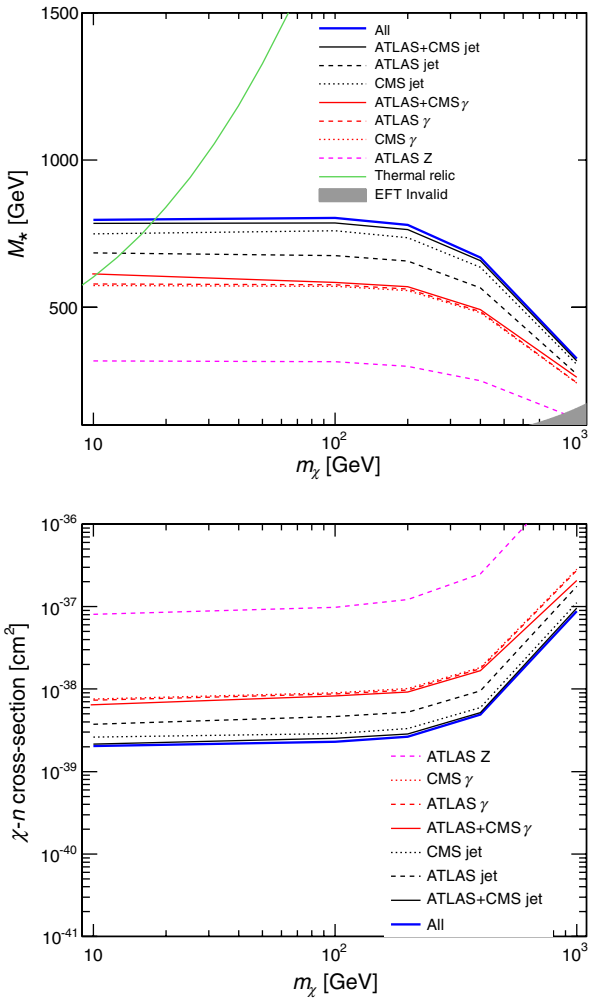

FIG. 3 (color online). Limits at 90% C.L. in $M_\star$ (top) and in the spin-independent WIMP-nucleon cross section (bottom) for individual and combined limits using the D5 operator as a function of m_χ.

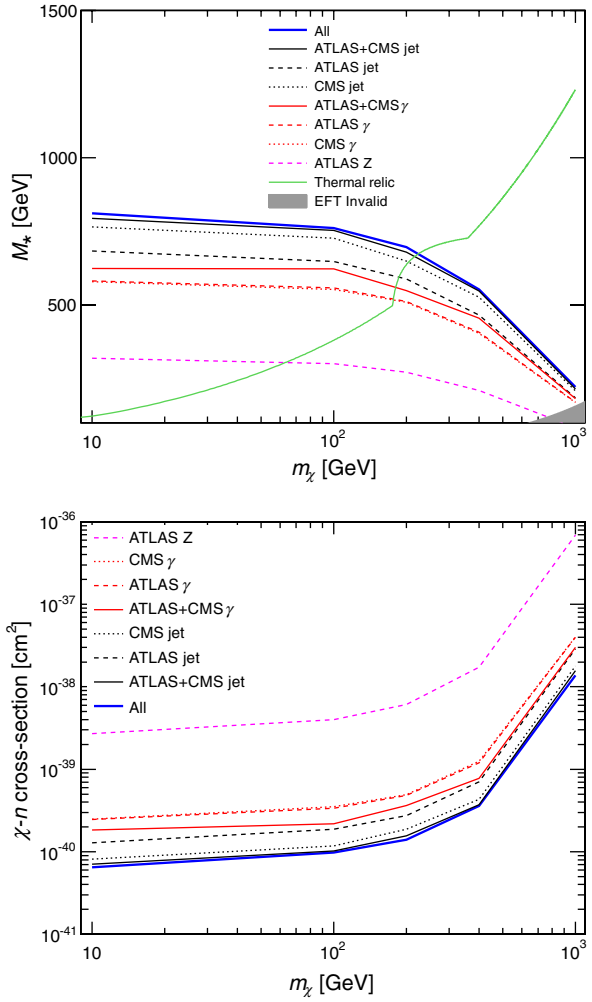

FIG. 4 (color online). Limits at 90% C.L. in $M_\star$ (top) and in the spin-dependent WIMP-nucleon cross section (bottom) for individual and combined limits using the D8 operator as a function of m_χ.

(i) the background uncertainties are monolithic and uncorrelated;

(ii) the signal selections are orthogonal.

Combining channels is then straightforward, although the intermediate step of a model-independent limit on the number of events N is no longer possible, as the limits depend on the relative distribution of signal events across channels, which is model-specific. Instead, cross-section limits are obtained directly. These limits are then converted into limits on $M_\star$, using the relationships from Ref. [14]. The individual-channel limits, combination across experiments and the grand combination of all channels are shown in Table V for the D5 operator and one choice of m_χ. Clearly the monojet analyses are the most powerful, and the greatest gain in combination is from combining the ATLAS and CMS monojet analyses, although the addition of the monophoton and mono-Z gives a non-negligible improvement in the combined result.

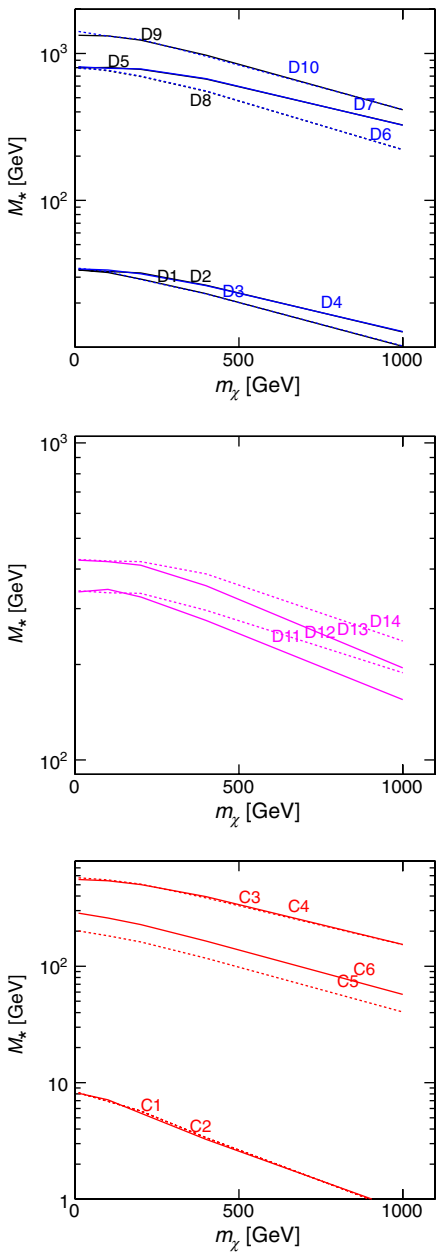

FIG. 5 (color online). Combined limits on $M_\star$ at 90% C.L., using all available channels, for operators D1–14 and C1–C5 as a function of m_χ.

Limits on $M_\star$ for the D5 and D8 operators are shown in Figs. 3 and 4 as well as limits on $\sigma(\chi - n)$. Where the $M_\star$ limits exceed the thermal relic values taken from Ref. [3], assuming that dark matter is entirely composed of thermal relics, the resulting dark matter density of the Universe would contradict WMAP measurements; therefore, WIMPs cannot couple to quarks or gluons exclusively via the given operator and account entirely for the relic density. This m_χ region is either excluded or requires that annihilation channels to leptons must exist or participation of different operators which interfere negatively, thereby reducing the limits on $M_\star$.

TABLE VI. Combined limits on $M_\star$ at 90% C.L., using all available channels, for operators D1–11 and C1–C5 for low and high values of the WIMP mass m_χ. Where possible, limits are shown on the WIMP-nucleon cross section, $\sigma(\chi - n)$.

Operator	m_χ (GeV)	$M_\star$ (GeV)	$\sigma(\chi - n)$ [cm^2]
D1	10	34	5.2×10^{-39}
	1000	10	8.3×10^{-36}
D2	10	34	
	1000	13	
D3	10	34	
	1000	10	
D4	10	34	
	1000	13	
D5	10	795	2.0×10^{-39}
	1000	325	8.8×10^{-38}
D6	10	791	
	1000	221	
D7	10	812	
	1000	324	
D8	10	811	6.5×10^{-41}
	1000	222	1.4×10^{-38}
D9	10	1331	8.9×10^{-42}
	1000	413	1.1×10^{-39}
D10	10	1410	
	1000	415	
D11	10	339	1.8×10^{-44}
	1000	155	2.4×10^{-42}
D12	10	342	
	1000	188	
D13	10	427	
	1000	195	
D14	10	429	
	1000	237	
C1	10	8	4.2×10^{-36}
	1000	1	6.1×10^{-36}
C2	10	8	
	1000	1	
C3	10	575	7.5×10^{-39}
	1000	153	1.8×10^{-36}
C4	10	556	
	1000	154	
C5	10	201	4.4×10^{-41}
	1000	41	3.1×10^{-42}
C6	10	286	
	1000	57	

IV. APPLICATION TO OTHER MODELS

While the experimental results are usually quoted for a small selection of the effective operator models, the analyses are clearly relevant for all of them.

We reinterpret the experimental analyses in the context of each operator and perform the grand combination across all channels. Figure 5 and Table VI show the limits on $M_\star$, translated to the WIMP-nucleon cross section where possible.

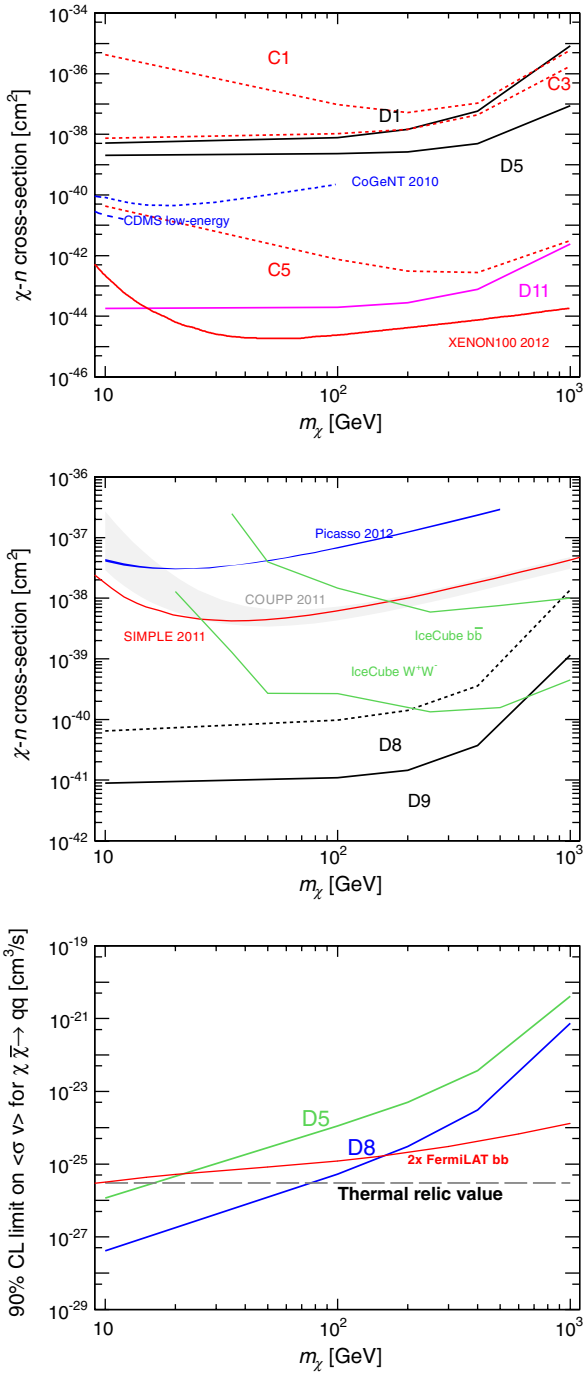

FIG. 6 (color online). Top and center: limits at 90% C.L. on the spin-independent and spin-dependent WIMP-nucleon cross section, $\sigma(\chi - n)$, for available operators. Bottom: interpretation of the limits on D5 and D8 in terms of the velocity-averaged WIMP-annhiliation cross section, as defined in Ref. [2].

In addition, we translate the limits on D5 and D8 into limits on the WIMP annihilation cross section; see Fig. 6.

V. CONCLUSIONS

We have presented the first combination of collider-based searches for dark matter pair production, using

final states involving jets, photons and leptonically decaying Z bosons in the context of effective field theories. The most powerful results are from the monojet analyses, and the greatest gains come from the combination of the independent analyses from ATLAS and CMS, although the other final states make a non-negligble improvement. The results are the strongest limits to date from collider searches in the effective field theory context.

In addition, we have reinterpreted the experimental results, quoted by ATLAS and CMS only for a few effective operators, across a broad range of operators, providing a comprehensive view of the power of these searches to constrain the weak-level or weaker

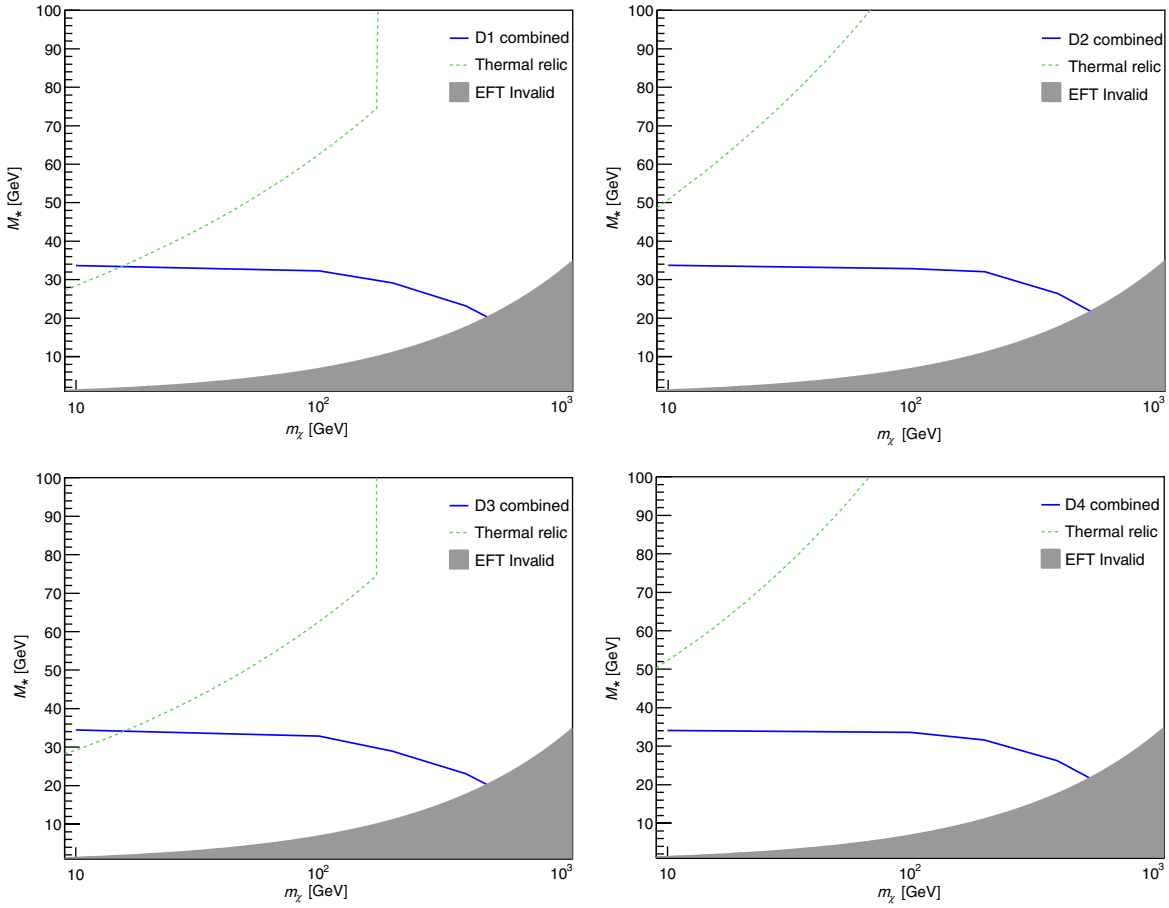

FIG. 7 (color online). Combined limits on $M_\star$ vs dark matter mass m_χ for operators D1, D2, D3 and D4. The $M_\star$ values at which dark matter particles of a given mass would result in the required relic abundance are shown as green dashed lines [3], assuming annihilation in the early Universe proceeded exclusively via the given operator.

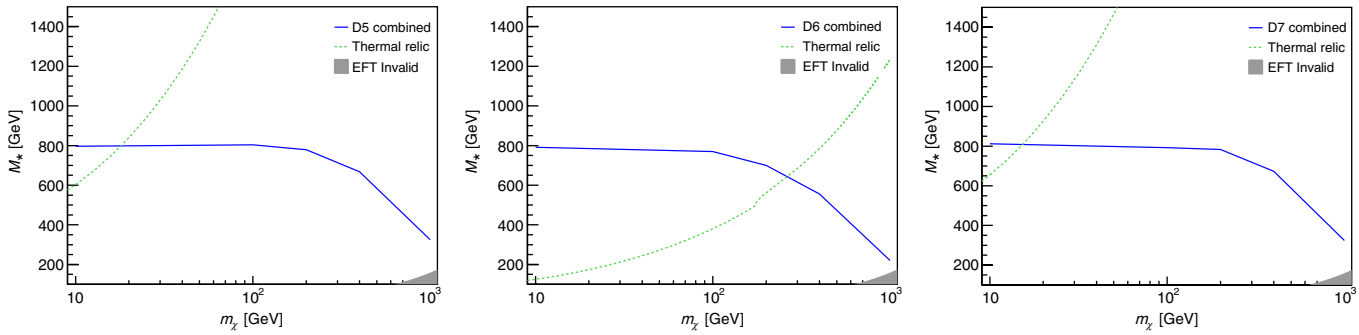

FIG. 8 (color online). Combined limits on $M_\star$ vs dark matter mass m_χ for operators D5, D6 and D7. The $M_\star$ values at which dark matter particles of a given mass would result in the required relic abundance are shown as green dashed lines [3], assuming annihilation in the early Universe proceeded exclusively via the given operator.

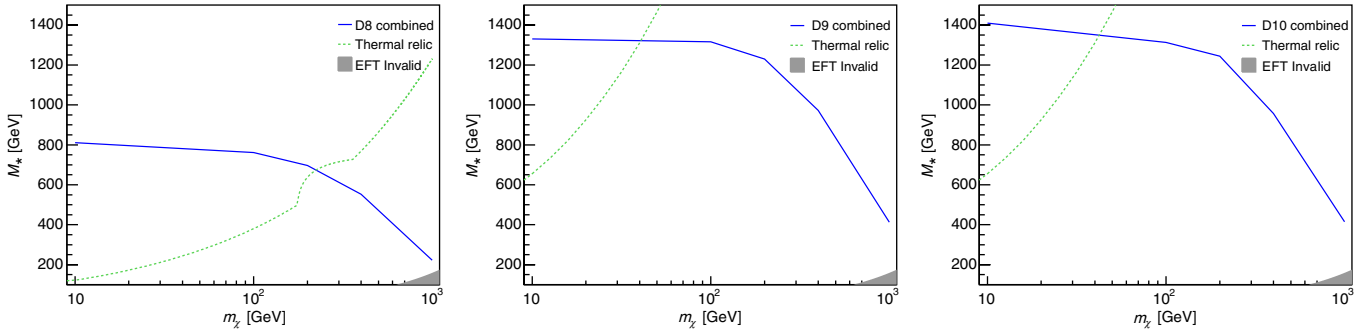

FIG. 9 (color online). Combined limits on $M_\star$ vs dark matter mass m_χ for operators D8, D9 and D10. The $M_\star$ values at which dark matter particles of a given mass would result in the required relic abundance are shown as green dashed lines [3], assuming annihilation in the early Universe proceeded exclusively via the given operator.

interactions between dark matter and standard model particles.

We have made use of the effective field theory framework to convert the ATLAS and CMS results to quantities relevant for direct-detection and indirect-detection dark matter searches. Under the assumptions made for the effective operators, LHC limits can be very competitive, in particular, for low-mass dark matter particles $m_\chi \leq 10$ GeV.

ACKNOWLEDGMENTS

We acknowledge useful conversations with Tim Tait, Roni Harnik, and Patrick Fox. D. W. and N. Z. are

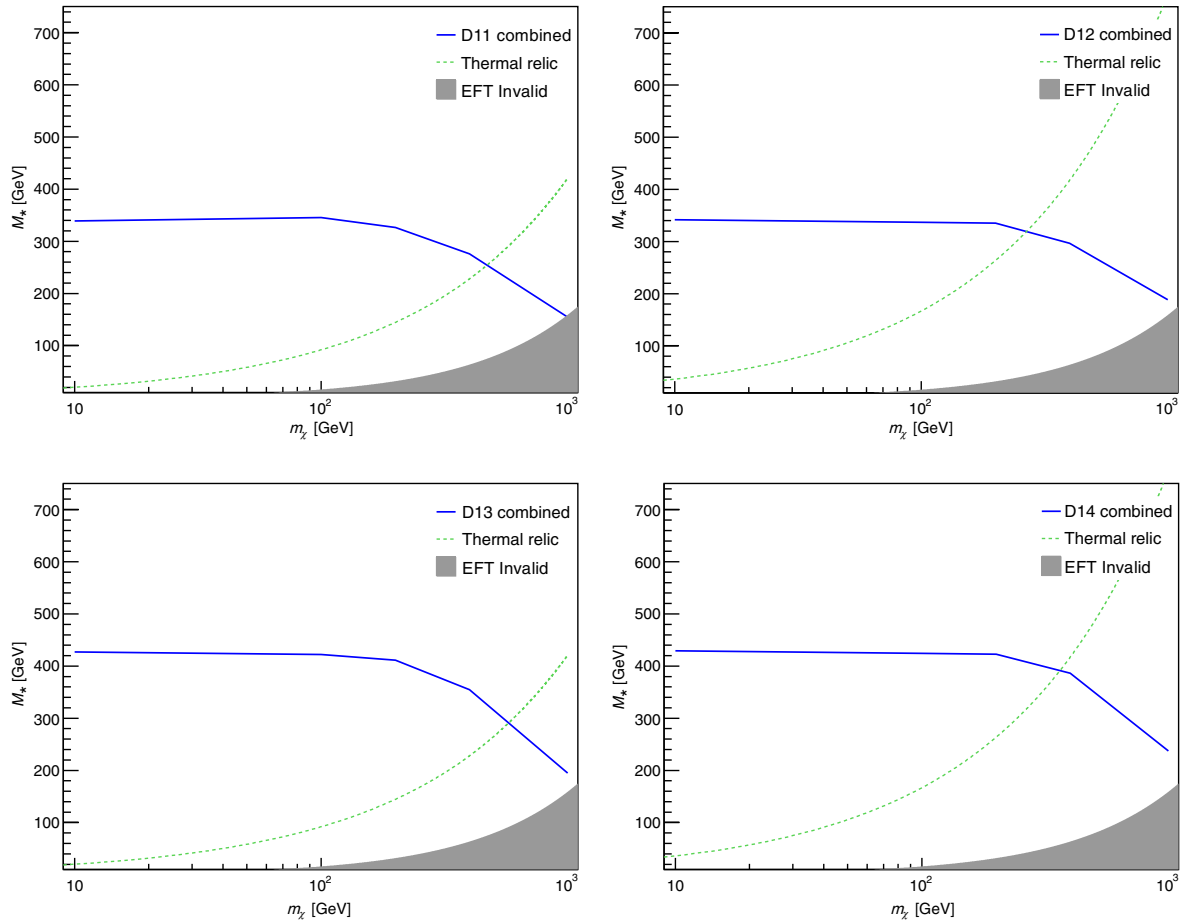

FIG. 10 (color online). Combined limits on $M_\star$ vs dark matter mass m_χ for operators D11, D12, D13 and D14. The $M_\star$ values at which dark matter particles of a given mass would result in the required relic abundance are shown as green dashed lines [3], assuming annihilation in the early Universe proceeded exclusively via the given operator.

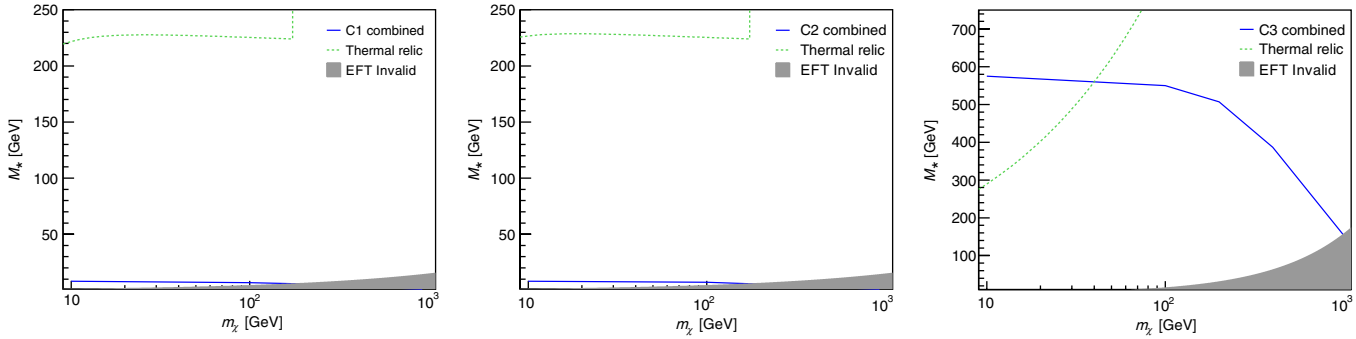

FIG. 11 (color online). Combined limits on $M_\star$ vs dark matter mass m_χ for operators C1, C2 and C3. The $M_\star$ values at which dark matter particles of a given mass would result in the required relic abundance are shown as green dashed lines [3], assuming annihilation in the early Universe proceeded exclusively via the given operator.

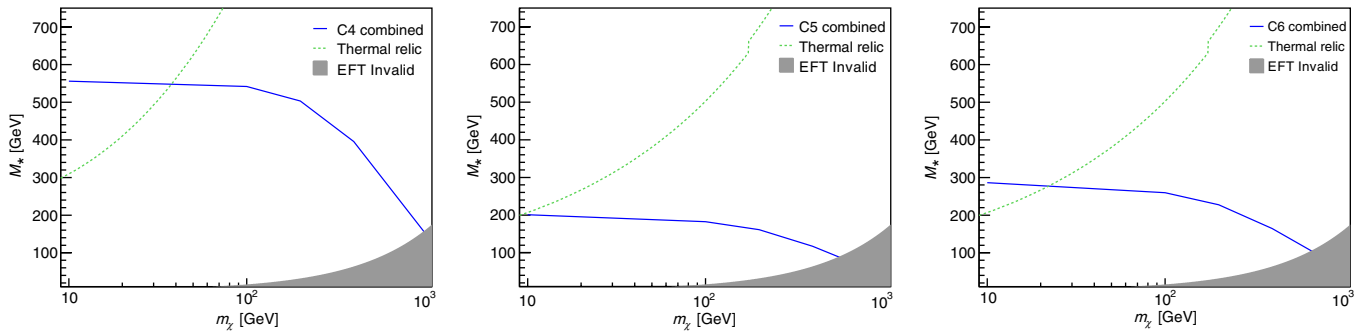

FIG. 12 (color online). Combined limits on $M_\star$ vs dark matter mass m_χ for operators C4, C5 and C6. The $M_\star$ values at which dark matter particles of a given mass would result in the required relic abundance are shown as green dashed lines [3], assuming annihilation in the early Universe proceeded exclusively via the given operator.

supported by grants from the Department of Energy Office of Science and by the Alfred P. Sloan Foundation.

APPENDIX: INDIVIDUAL OPERATORS

In Figs. 7–12, we show the combined limits for each operator, compared to the thermal relic values. Where the limits exceed the thermal relic values, assuming that dark matter is entirely composed of thermal relics, the dark matter density of the Universe would contradict measurements and hence cannot couple to quarks or gluons exclusively via the given operator. This m_χ region is either excluded, else other annihilation channels to leptons must exist, or finally different operators may interfere negatively thereby reducing the limits on $M_\star$.

[1] M. Beltran, D. Hooper, E. W. Kolb, Z. A. C. Krusberg, and T. M. P. Tait, J. High Energy Phys. 09 (2010) 037.
[2] P. J. Fox, R. Harnik, J. Kopp, and Y. Tsai, Phys. Rev. D **85**, 056011 (2012).
[3] J. Goodman, M. Ibe, A. Rajaraman, W. Shepherd, T. M. P. Tait, and H.-B. Yu, Phys. Rev. D **82**, 116010 (2010).
[4] G. Aad *et al.* (ATLAS Collaboration), J. High Energy Phys. 04 (2013) 075.
[5] S. Chatrchyan *et al.* (CMS Collaboration), J. High Energy Phys. 09 (2012) 094.
[6] G. Aad *et al.* (ATLAS Collaboration), Phys. Rev. Lett. **110**, 011802 (2013).
[7] S. Chatrchyan *et al.* (CMS Collaboration), Phys. Rev. Lett. **108**, 261803 (2012).
[8] Y. Bai and T. M. P. Tait, arXiv:1208.4361.
[9] G. Aad *et al.* (ATLAS Collaboration), J. High Energy Phys. 03 (2013) 128.
[10] L. M. Carpenter, A. Nelson, C. Shimmin, T. M. P. Tait, and D. Whiteson, Phys. Rev. D **87**, 074005 (2013).
[11] M. Beltran, D. Hooper, E. W. Kolb, and Z. C. Krusberg, Phys. Rev. D **80**, 043509 (2009).

[12] W. Shepherd, T. M. P. Tait, and G. Zaharijas, Phys. Rev. D **79**, 055022 (2009).
[13] Q.-H. Cao, C.-R. Chen, C. S. Li, and H. Zhang, J. High Energy Phys. 08 (2011) 018.
[14] J. Goodman, M. Ibe, A. Rajaraman, W. Shepherd, T. M. P. Tait, and H.-B. Yu, Phys. Lett. B **695**, 185 (2011).
[15] Y. Bai, P. J. Fox, and R. Harnik, J. High Energy Phys. 12 (2010) 048.
[16] A. Rajaraman, W. Shepherd, T. M. P. Tait, and A. M. Wijangco, Phys. Rev. D **84**, 095013 (2011).
[17] R. C. Cotta, J. L. Hewett, M. P. Le, and T. G. Rizzo, arXiv:1210.0525.
[18] F. J. Petriello, S. Quackenbush, and K. M. Zurek, Phys. Rev. D **77**, 115020 (2008).
[19] Y. Gershtein, F. Petriello, S. Quackenbush, and K. M. Zurek, Phys. Rev. D **78**, 095002 (2008).
[20] P. J. Fox, R. Harnik, R. Primulando, and C.-T. Yu, Phys. Rev. D **86**, 015010 (2012).
[21] K. Cheung, P.-Y. Tseng, Y.-L. S. Tsai, and T.-C. Yuan, J. Cosmol. Astropart. Phys. 05 (2012) 001.
[22] N. F. Bell, J. B. Dent, A. J. Galea, T. D. Jacques, L. M. Krauss, and T. J. Weiler, Phys. Rev. D **86**, 096011 (2012).
[23] P. J. Fox and C. Williams, Phys. Rev. D **87**, 054030 (2013).
[24] I. M. Shoemaker and L. Vecchi, Phys. Rev. D **86**, 015023 (2012).
[25] J. Alwall, M. Herquet, F. Maltoni, O. Mattelaer, and T. Stelzer, J. High Energy Phys. 06 (2011) 128.
[26] A. Read, J. Phys. G **28**, 2693 (2002).
[27] T. Junk, Nucl. Instrum. Methods Phys. Res., Sect. A **434**, 435 (1999).